Journal of Materials Chemistry A

Accepted Manuscript

ROYAL SOCIETY OF CHEMISTRY

www.rsc.org/materialsA

Concave Bi_2WO_6 nanoplates with oxygen vacancies achieving enhanced electrocatalytic oxygen evolution in near-neutral water

Zhu-Ping Nie, [a] De-Kun Ma, *[a] Guo-Yong Fang, [ab] Wei Chen [a] and Shao-Ming Huang *[a]

Abstract:

Developing highly efficient and inexpensive oxygen evolution reaction (OER) electrocatalyst in near-neutral water is of paramount importance for many practical applications. Herein, we report that Bi_2WO_6 concave nanoplates (CNPs) with oxygen vacancies enable electrocatalytic OER under neutral conditions with high activity and good durability. To the best of our knowledge, this is the first example on W-based electrocatalyst containing no first-row transition metal or precious metal elements for OER in near-neutral water. Experimental results and first-principles calculations revealed that the presence of oxygen vacancies in Bi_2WO_6 CNPs could significantly decrease charge-transfer resistance and adsorption barrier of H_2O molecules in the process of electrochemistry, and thus benefiting the improvement of OER activity. The fabrication of concave surfaces with high energy facets could further enhance OER activity of the Bi_2WO_6 NPs electrocatalysts. As a result, the synergistic effect of oxygen vacancies and concave surfaces endowed impressive performance of Bi_2WO_6 CNPs for OER, which is comparable to the best electrocatalysts among known inorganic non-precious metal compounds. The present strategy on the combination of defect and crystal facet engineering could open a new avenue to design new and highly efficient OER electrocatalysts.

1. Introduction

The depletion of fossil fuels and the associated adverse impact on environment have triggered

[a] Nanomaterials and Chemistry Key Laboratory, Wenzhou University, Wenzhou, Zhejiang 325027, P. R. China

[b] National Laboratory of Solid State Microstructures, College of Engineering and Applied Sciences, Nanjing University, Nanjing 210093, China

*Corresponding authors: dkma@wzu.edu.cn; smhuang@wzu.edu.cn. Fax: +86-577-8837-3017; Tel: +86-577-8837-3031.

† Electronic supplementary information (ESI) available. See DOI:

much attention for sustainable energy conversion and storage systems.[1-3] Recently, the oxygen evolution reaction (OER) has attracted great research interest because of its critical role in variously promising energy conversion and storage technologies, such as photocatalytic or electrocatalytic water splitting for hydrogen production,[4] regenerative fuel cells,[5] rechargeable metal-air batteries,[6] and many more.[7] As far as electrocatalytic water splitting is concerned, its reaction rate is mainly determined by complex and kinetically sluggish of OER.[8] Therefore a highly efficient OER electrocatalyst is required to address the kinetically slow process. Although IrO_2 and RuO_2 display excellent electrocatalytic performance for OER, severe scarcity and high cost hampered their extensive applications. Accordingly, various non-precious-metal catalysts have been developed as competitive alternatives, typically including first-row spinel and perovskite metal oxides and their derivatives,[9-12] layered double hydroxides,[13] carbon-based nonmetal catalysts,[14] as well as some transition metal complexes.[15] However, usually, the above catalysts need to be performed in concentrated basic ($pH \geq 13$) or acidic ($pH \leq 1$) solutions.[16] Up to now, only a few catalysts can efficiently operate OER in near-neutral water under ambient conditions.[17-22] The development of earth-abundant catalysts that run OER under benign conditions remains a great challenge.

As one of the simplest members of the Aurivillius family, Bi_2WO_6 with a layered structure is composed of perovskite-like slab of $[WO_4]^{2-}$ sandwiched between bismuth oxide $[Bi_2O_2]^{2+}$ units. Relatively narrowed band gap (2.8 eV), appropriate energy band positions, and favorable separation of photogenerated electron-hole pairs caused by internal electric fields between the slabs make Bi_2WO_6 particularly suitable for the photocatalytic or photoelectrocatalytic degradation of organics,[23,24] selective organic synthesis and production of fuels.[25] As a result, many efforts have been made to enhance photocatalytic activity of Bi_2WO_6 through the fabrication of special nanostructures, doping, substitution, and surface modification.[26] However, until now, concave Bi_2WO_6 nanoplates and Bi_2WO_6 CNPs as an efficient electrocatalyst for OER in near-neutral water have never been reported.

In some cases, oxygen vacancies can improve the conductivity of the materials and decrease the adsorption barrier of H_2O molecules onto its surfaces and thus will be given enhanced electrocatalytic activity.[27-29] On the other hand, crystals with concave surfaces possess open negative curvatures and high-index facets, which are expected to show significantly enhanced

catalytic activity relative to their flat and convex counterparts.[30-34] Herein, inspired by the above considerations, Bi_2WO_6 CNPs with oxygen vacancies have been synthesized for the first time. Importantly, the Bi_2WO_6 CNPs with oxygen vacancies enable electrocatalytic water oxidation under near-neutral conditions with high activity and good stability. Our work opens a new avenue into the design of highly active and stable OER electrocatalysts.

2. Experimental Section

Synthesis of Bi_2WO_6 CNPs. In a typical procedure, 0.5 mmol of $Bi(NO_3)_3 \cdot 5H_2O$ was added to 15 mL of absolute alcohol under stirring for 15 min at room temperature. Afterward, 20 mL of aqueous solution containing 1 mmol of $Na_2WO_4 \cdot 2H_2O$ and 5 mL of oleylamine were added into the above solution. The mixture was finally transferred into a 50 mL of Teflon-lined autoclave and maintained at 220 ^oC for 6 h. The reactor was cooled to room temperature naturally. The resulting sample was collected and washed for several times with alcohol and deionized water and dried at 60 ^oC under vacuum.

Materials Characterization. Powder X-ray diffraction (XRD) was performed on a Bruker D8 Advance X-ray diffractometer using Cu Kα radiation (λ = 0.15418 nm) at a scanning rate of 8°/min in the 2θ range of 10-70°. Field-emission scanning electron microscopy (FE-SEM) images were taken on a Nova NanoSEM200 scanning electron microscope. Transmission electron microscopy (TEM) image, high-resolution transmission electron microscopy (HRTEM) image, scanning transmission electron microscopy (STEM) image, energy dispersive X-ray spectroscopy (EDS), and elemental mapping were carried out on a JEM-2100F HRTEM, using an accelerating voltage of 200 kV. The UV-vis diffuse-reflectance spectra (UV-DRS) were recorded on a UV2501PC (Shimadzu) using $BaSO_4$ as a reference. X-ray photoelectron spectroscopy (XPS) measurement was carried out with a Thermo ESCALAB 250 X-ray photoelectron spectrometer with an excitation source of Al Kα radiation (λ = 1253.6 eV). The Brunauer-Emmett-Teller (BET) surface area was measured with an ASAP2020 specific surface area analyzer.

Preparation of Working Electrode. 5 mg of the as-synthesized Bi_2WO_6 CNPs was dispersed in 1 mL of isopropyl alcohol and ultrapure water mixture ($V_{isopropyl\ alcohol}$: V_{water} = 2 : 1) by at least 30 min sonication. Then 40 μL of naphthol was added in the solution. After another 30 min sonication, a homogenous ink was formed. After that, 5 μL of the catalyst ink was loaded onto a

glassy carbon electrode of 3 mm in diameter (loading 0.34 mg cm^{-2}).

Electrochemical Properties Measurements. All electrochemical experiments were carried out on an electrochemical system (CHI660D) in a three-electrode cell using Bi_2WO_6 CNPs/GC as the working electrode, a Pt wire as the counter electrode and saturated calomel electrode (SCE) as the reference electrode, respectively. Electrolyte was 0.5 M Na_2SO_4 whose pH is 6.6. Electrode potential was converted to the RHE scale, using the following equation: E(RHE) = E(SCE) + 0.242 + 0.059 × pH. Electrochemical impedance spectra were carried out using above three electrode systems. The frequency range was 100 K Hz to 0.1 Hz, and the amplitude of the applied voltage was 5 mV.

3. Results and Discussion

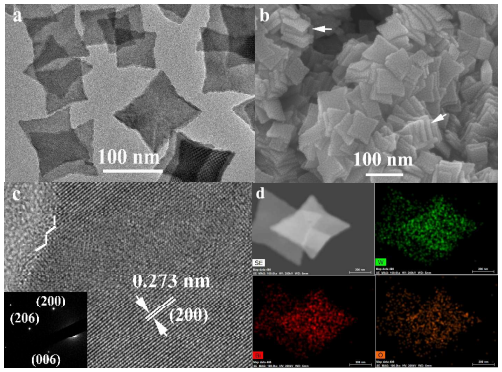

Fig. 1 TEM image (a) and FE-SEM image (b) of the synthesized Bi_2WO_6 CNPs. HRTEM image (c) recorded on the rim of a Bi_2WO_6 CNP and its corresponding SAED pattern as inserted. STEM image and elemental mapping of Bi_2WO_6 CNPs (d). Green, red, and orange represent W, Bi, and O elements, respectively.

Bi_2WO_6 CNPs were synthesized by a facile one-pot solvothermal route. As can be seem from TEM image in Fig. 1a, the as-obtained products are CNPs with an average side length of about 80 nm. The X-ray diffraction pattern of the products could be indexed to the orthorhombic phase of Bi_2WO_6 (JCPDS No. 73-1126, see Fig. S2). No diffraction peaks from Bi_2O_3, WO_3 and other substances were observed, suggesting that the products have high purity. The thickness of Bi_2WO_6 nanoplate is *ca*. 20 nm, measured from the nanoplates in FE-SEM image (marked with white arrowheads, Fig. 1b). Both HRTEM image and selected-area electron diffraction pattern recorded

on the individual nanoplate show its single-crystalline structure (Fig. 1c). HRTEM observations also indicate that the nanoplate has good crystallinity. The distinct lattice fringe spacing of 0.273 nm matches well the interplanar separation of (200) planes of orthorhombic Bi_2WO_6. Especially, as seen from HRTEM image of the Bi_2WO_6 CNP, there are a number of atomic terraces and steps on its brims (marked with white lines in Fig. 1c), indicating that the Bi_2WO_6 nanoplate are enclosed by high-index facets (for detailed proof see Supporting Information, Fig. S3).[31-33] STEM-EDS elemental maps of the nanoplates were further used to identify the element distribution. As shown in Fig. 1d, three elements of W, Bi, and O are homogeneously distributed throughout the Bi_2WO_6 CNPs. The quantitative calculation from EDX spectrum of the Bi_2WO_6 CNPs shows that the ratio of Bi to W is close to stoichiometric 2 : 1 (Fig. S4).

It has been acknowledged that the formation of crystals with concave surfaces is not favored by thermodynamics because of the higher surface energy and inner strain.[32] In the present reaction system, oleylamine (OLA) plays a key role to control the shape and exposed facets. In the absence of OLA, keeping other synthetic conditions unchanged, only three-dimensional hierarchical microspheres were obtained (Fig. S5). According to time-dependent XRD analyses and SEM observations on the intermediates (Fig. S6 and Fig. S7), the formation of Bi_2WO_6 CNPs went through anisotropic growth of nanoparticles and Ostwald ripening process of concave nanoplates. As previous reported, here OLA molecules also played a role of capping reagents.[33] They could selectively adsorb on the surfaces of newborn Bi_2WO_6 nanoparticles and induce the preferential overgrowth, thus favoring the formation of CNPs. Interestingly, the morphology of CNPs still kept unchanged after the amounts of reactants were increased by three times and gram-scale products could be easily prepared through one-pot reaction (Fig. S8).

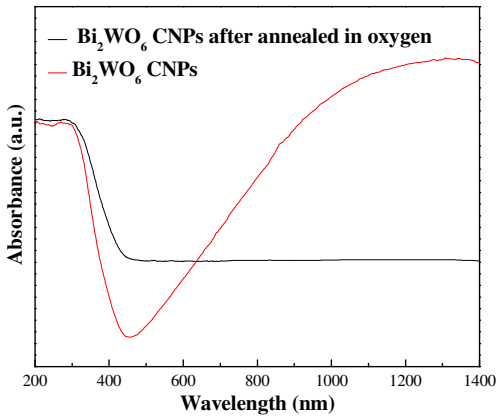

Fig. 2 UV-visible diffuse reflectance spectra of Bi_2WO_6 CNPs before and after annealing in oxygen.

The as-obtained Bi_2WO_6 CNPs powder exhibits a unique bluish-gray color, which is quite different from previous report (yellow appearance).[35] UV-visible diffuse reflectance spectroscopy of the sample shows strong absorption in the regions of 200-400 and 550-1400 nm (Fig. 2), which is consistent with its bluish-gray appearance (Fig. S8). Usually, oxygen vacancies can cause some metal oxides strong near-infrared light absorption.[36] Most recently, the theoretical calculation has shown that the 72-atom super cell of Bi_2WO_6 possesses three oxygen vacancies.[37] Therefore it suggests that the as-prepared Bi_2WO_6 CNPs with strong near-infrared light absorption contain oxygen vacancies. In order to confirm this point, XPS studies on the Bi_2WO_6 CNPs were carried out. Fig. 3a, 3b and 3c represent high resolution spectra of Bi 4f, W 4f and O 1s, respectively. As shown in Fig. 3a, the spin-orbit components of Bi 4f5/2 and Bi 4f7/2 consist of peaks with binding energy around 164.2 and 159.0 eV, respectively, which is in agreement with Bi^{3+} ions in Bi_2WO_6.[38] The W 4f core-level spectrum could be fitted into spin-orbit doublets (Fig. 3b), corresponding to two different oxidation state of W atoms. The dominant peaks at 37.5 and 35.3 eV can be assigned to the emission of W 4f5/2 and W 4f7/2 core level from the atoms with W^{6+} oxidation state, while the other two weaker peaks located at 36.2 and 34.2 eV correspond to lower +5 valence of W.[37] The binding energy of W 4f for the sample after calcinated in oxygen obviously increases, which also supports the existence of W^{5+} in Bi_2WO_6 CNPs (Fig. 3d). The presence of low valence W in tungsten oxides is often associated with oxygen vacancies.[36] The further analysis on O 1s core level spectrum could also confirm this point. Specifically, the peak at 529.8 eV is due to oxygen atoms bound to metals, while the peak at 531.1 eV is attributed to a high number of defect sites with a low oxygen coordination, namely, oxygen vacancy.[28] In addition, near-infrared light absorption of Bi_2WO_6 CNPs disappeared after they were thermally treated in oxygen atmosphere (Fig. 2), which also supported the presence of oxygen vacancies.

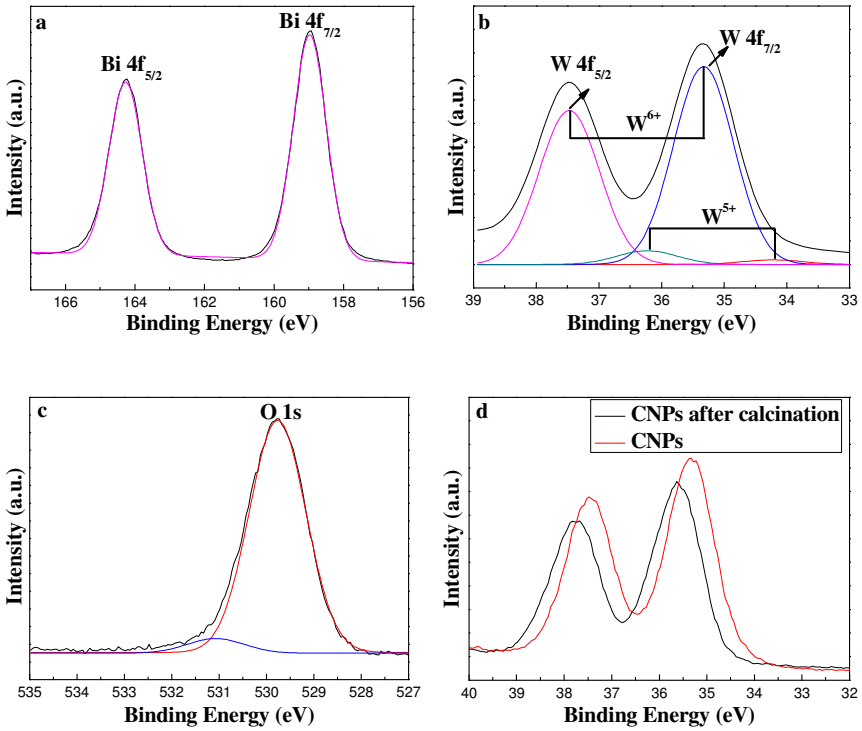

Fig. 3 High resolution XPS spectra of Bi 4f (a), W 4f (b), and O 1s (c). The comparison of W 4f spectra of Bi_2WO_6 CNPs and Bi_2WO_6 CNPs after calcinated in oxygen (d).

The OER activities of the as-prepared Bi_2WO_6 CNPs were then systematically investigated. The sample was loaded onto glass carbon (GC) electrode (the loading amount was *ca*. 0.34 mg cm^{-2}) in 0.5 M Na_2SO_4 aqueous solution (pH = 6.6) with a scan rate of 10 mV s^{-1} using a three-electrode system. For comparison, similar measurements for bare GC and Bi_2WO_6 CNPs after calcination in oxygen with same loading amounts were also performed. Fig. 4a shows their linear sweep voltammetry (LSV) curves without ohmic potential drop (iR) losses correction on the reversible hydrogen electrode (RHE) scale. It can be seen that the Bi_2WO_6 CNPs/GC electrode exhibits much greater current density compared with Bi_2WO_6 CNPs after calcination/GC and bare GC ones under a certain applied voltage, directly confirming that Bi_2WO_6 CNPs possess the highest electrocatalytic activity for OER among them. Specifically, the current density of Bi_2WO_6 CNPs can reach 10 mA cm^{-2} (a metric relevant to solar fuel production) at an applied voltage of 1.77 V vs RHE, which is approximately 20 times larger than that of Bi_2WO_6 CNPs after calcination counterpart (*ca*. 0.5 mA cm^{-2}). Moreover, Bi_2WO_6 CNPs exhibit a relatively small overpotential of 0.37 V for electrocatalytic O_2 evolution. Considering the onset overpotential and

catalytic current densities together, Bi_2WO_6 CNPs represent one of the best electrocatalysts for OER in near-neutral water without involving any noble metal or first-row transition metal elements (Fig. 4b, Table S1). Furthermore, we assessed the long-term electrochemical stability of this electrode for OER under near-neutral condition through cyclic voltammogram tests (Fig. 4c). The polarization curves recorded before and after 500 cycles were compared. As observed, the OER activity of Bi_2WO_6 CNPs showed negligible change, indicating good durability of the Bi_2WO_6 CNPs catalyst.

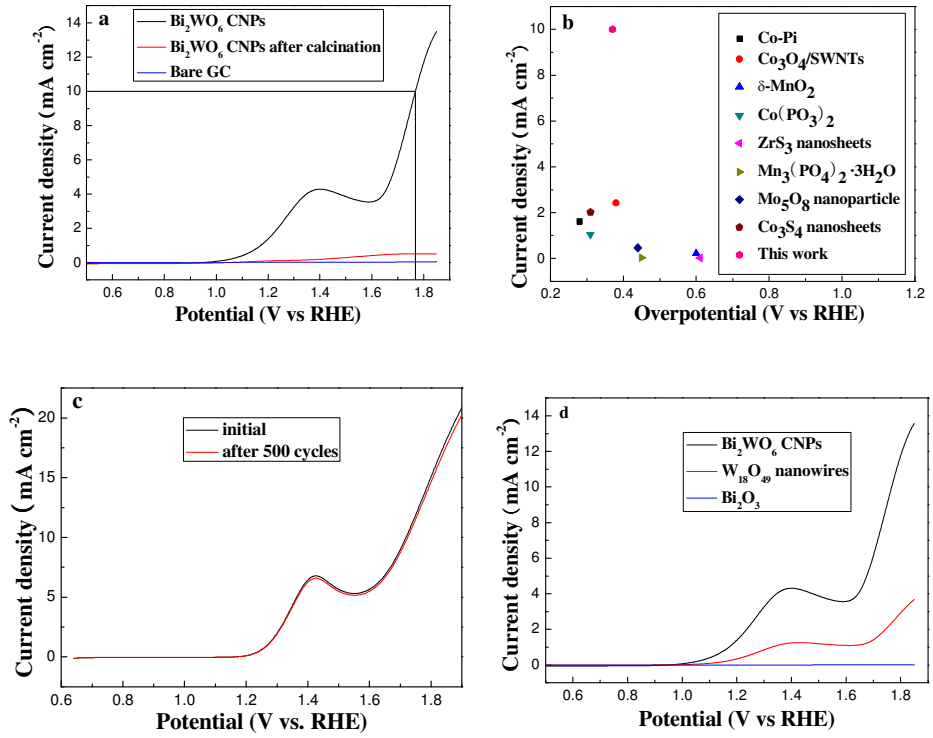

Fig. 4 LSV curves for Bi_2WO_6 CNPs, Bi_2WO_6 CNPs after annealing in O_2, and bare GC in neutral Na_2SO_4 solution with a scan rate of 10 mV s^{-1} (a). The current density (at an overpotential of 0.54 V) and onset overpotential of some typical inorganic OER electrocatalysts (b). LSV curves for Bi_2WO_6 CNPs/GC electrode before and after 500 cycles (c). LSV curves for Bi_2WO_6 CNPs, $W_{18}O_{19}$ nanowires, and rod-like Bi_2O_3 (d).

Bi_2WO_6 is constructed of perovskite-like $(WO_4)^{2-}$ and alternating $(Bi_2O_2)^{2+}$ units. In order to understand the active site of Bi_2WO_6 CNPs, both rod-like Bi_2O_3 and $W_{18}O_{49}$ nanowires containing oxygen vacancies were prepared according to previous reports (Supporting Information, Fig. S9-12).[39, 36] Following the same preparation conditions as that of Bi_2WO_6 CNPs/GC electrode, the

obtained Bi_2O_3 and $W_{18}O_{49}$ were respectively fabricated into electrodes for further electrochemical studies. As shown in Fig. 4d, Bi_2O_3 with oxygen vacancies shows negligible activity for OER, while the current density of $W_{18}O_{49}$ containing oxygen vacancies can reach 2.42 mA cm^{-2} at an overpotential of 0.54 V. On the other hand, in LSV curves of Bi_2WO_6 CNPs (Fig. 4a) and $W_{18}O_{49}$ nanowires (Fig. 4d), they show similar anodic peaks located at *ca*. 1.41 V vs. RHE, which are probably ascribed to low valent W to high valent one. The above results suggest that the electrocatalytic activity of Bi_2WO_6 CNPs originates from perovskite-like slab of $[WO_4]^{2-}$. In order to further support this conclusion, a catalyst poisoning test was carried out on the assumption that the catalytic active center was located at $(Bi_2O_2)^{2+}$ slab. Potassium tartrate can form stable bismuth potassium tartrate complex with Bi^{3+} ions on the surfaces of Bi_2WO_6 CNPs and thus will poison the OER activity of Bi_2WO_6 CNPs. When a certain amount of potassium tartrate was added into Na_2SO_4 electrolyte solution, on the contrary, the resultant OER activity almost kept unchanged (Fig. S13). This result shows that the catalytic active center of Bi_2WO_6 CNPs originates from $[WO_4]^{2-}$ slab rather than $(Bi_2O_2)^{2+}$ layer. Considering to electrochemically active surface area (ECSA) of $W_{18}O_{49}$ nanowires was 2.6-times larger than that of Bi_2WO_6 CNPs (see supporting information, Fig. S14), while the catalytic current density for the latter is higher than the former. Therefore we can conclude that the intrinsic electrocatalytic activity of Bi_2WO_6 CNPs is obviously superior to that of $W_{18}O_{49}$ nanowires.

Oxygen vacancies played key roles in enhancing OER activity of Bi_2WO_6 CNPs. As above mentioned analyses, oxygen vacancies are related to low valent W, which is manifested by strong absorption in near-infrared region. Therefore the concentration of oxygen vacancies could be adjusted by controlled oxidation reaction between low valent W and appropriate oxidant such as H_2O_2.[36] To be specific, 100 mg of Bi_2WO_6 CNPs was treated with 40 mL of H_2O_2 solution with concentrations of 3.75 (sample 1) , 15 (sample 2), 30 (sample 3), and 60 mg/mL (sample 4) for 1 h, respectively. As UV-vis absorption spectra shown in Fig. 5a, the absorbance in near-infrared region gradually declined for Bi_2WO_6 CNPs after treatments with increasing the amount of H_2O_2. The results show that the oxygen vacancies on the surfaces of the Bi_2WO_6 CNPs gradually decreased with increasing consumption of H_2O_2. The corresponding Bi_2WO_6 CNPs with different amounts of oxygen vacancies displayed distinct OER activities. As shown in Fig. 5b, fewer oxygen vacancies Bi_2WO_6 CNPs have, weaker OER activity they show. Usually, more oxygen

vacancies can collect more electrons and lead to enhanced conductivity of the material.[28] The electrochemical impedance of Bi_2WO_6 CNPs with different amounts of oxygen vacancies further confirmed this point. As shown in Fig. 5c, the Nyquist plots indicate that the charge-transfer resistance of Bi_2WO_6 CNPs varied with the amounts of oxygen vacancies. Untreated Bi_2WO_6 CNPs with the largest content of oxygen vacancies exhibited the smallest charge-transfer resistance. With decreasing oxygen vacancies controlled through the treatment of increasing H_2O_2 doses, the resultant Bi_2WO_6 CNPs showed larger and larger charge-transfer resistance. Therefore the presence of oxygen vacancies really benefits the transfer of charge. On the other hand, the oxygen vacancies on the surfaces of Bi_2WO_6 CNPs also favor the adsorption of H_2O molecules. In order to illuminate this point, the adsorption energy of H_2O molecules on a perfect surface and a surface with one oxygen vacancy was calculated based on density functional theory (DFT) model (Fig. 5d, detailed method see Supporting Information). As a result, the adsorption energy of H_2O molecules on a surface with one oxygen vacancy is 29.5 kcal/mol, obviously larger than that of H_2O molecules on a perfect surface (14.5 kcal/mol). This means that Bi_2WO_6 CNPs with oxygen vacancies are more favorable for adsorbing H_2O molecules. This feature is conducive to OER because the adsorption of H_2O is a rate-determining process.

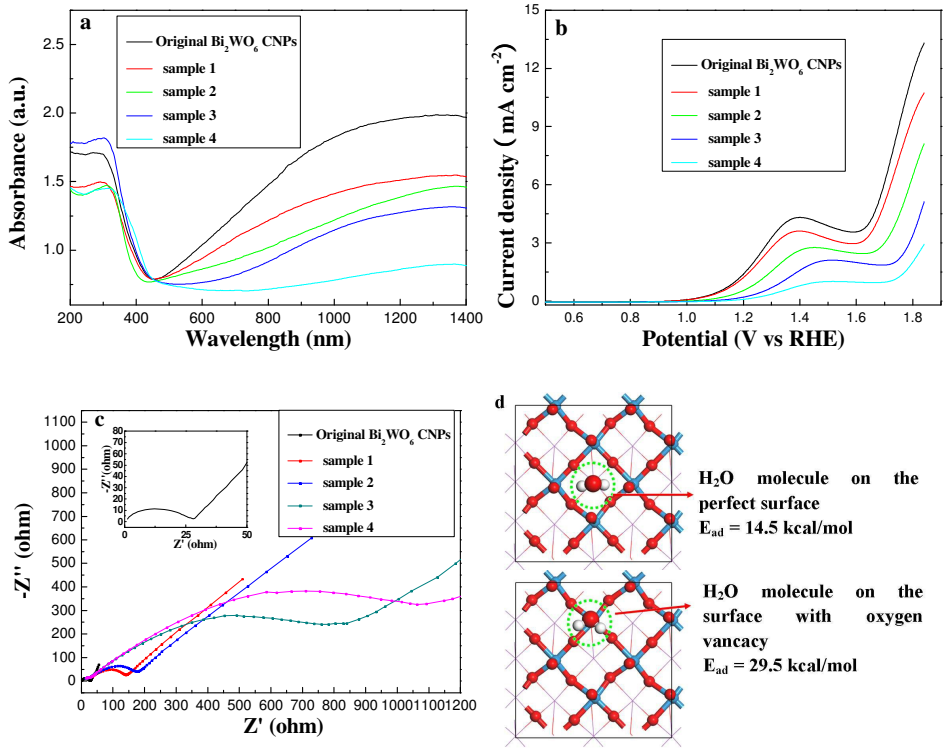

Fig. 5 UV-visible diffuse reflectance spectra (a), LSV curves (b), and electrochemical impendence spectra (c) of original Bi_2WO_6 CNPs and Bi_2WO_6 CNPs after treated with different concentrations of H_2O_2 solution (Sample 1-4). Inset in Fig. 5c: electrochemical impendence spectrum of original Bi_2WO_6 CNPs. Adsorption models of H_2O molecule on a perfect surface and a surface with one oxygen vacancy (d).

The good OER activity was also attributed to exposed high energy facets on the surfaces of Bi_2WO_6 CNPs except for oxygen vacancies. In order to demonstrate this point, flat Bi_2WO_6 nanoplates containing oxygen vacancies were synthesized through a modified hydrothermal route.[40] Compared with Bi_2WO_6 CNPs, the obtained flat Bi_2WO_6 nanoplates have a similar side length but thinner thickness (15 nm, Fig. S15 and S16). Flat Bi_2WO_6 nanoplates have a 4.2-times larger ECSA compared with Bi_2WO_6 CNPs (Fig. S17). The flat Bi_2WO_6 nanoplates also have higher oxygen vacancies contents than Bi_2WO_6 CNPs after treated with 40 mL of H_2O_2 (60 mg/mL), roughly estimated from their corresponding UV-vis absorption spectra in near-infrared region (Fig. S18). Although larger ECSA and higher oxygen vacancies contents, flat Bi_2WO_6 obviously exhibited lower OER activity than the Bi_2WO_6 CNPs sample treated with H_2O_2 (Fig. 6). To be specific, at an applied voltage of 1.77 V vs RHE, the current density of Bi_2WO_6 CNPs after treated with H_2O_2 (1.47 mA cm^{-2}) is 3 times larger than that of flat Bi_2WO_6 nanoplates (0.49 mA cm^{-2}). These results clearly show that the fabrication of concave facets with high energy facets can significantly enhance OER activity of electrocatalyst.

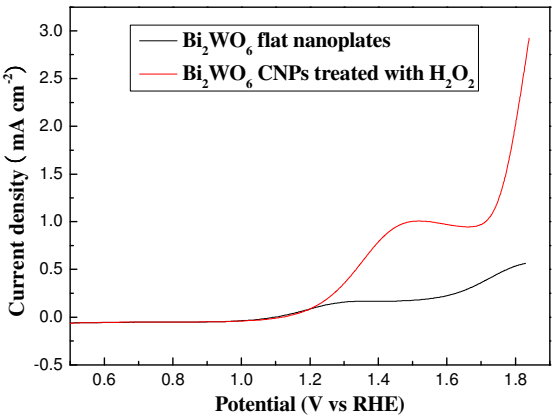

Fig. 6 LSV curves of Bi_2WO_6 nanoplates and Bi_2WO_6 CNPs after treated with 40 mL of H_2O_2 (60 mg/mL).

4. Conclusion

In summary, we have reported Bi_2WO_6 CNPs with oxygen vacancies as a new electrocatalyst for efficient water oxidation under near-neutral condition for the first time. From experimental results, the presence of oxygen vacancies in Bi_2WO_6 CNPs could greatly reduce charge-transfer resistance in the process of electrochemical reaction. Based on the theoretical calculations, the oxygen vacancies on the surfaces of Bi_2WO_6 CNPs favor the adsorption of H_2O molecules and decrease the OER barrier, resulting in improved water oxidation activity. On the other hand, the concave surfaces with high energy crystalline facets considerably enhanced electrocatalytic activity of Bi_2WO_6 nanoplates. As a result, the synergistic effect of oxygen vacancies and concave surfaces endowed impressive performance of Bi_2WO_6 CNPs for OER with a large current density at relatively small overpotential and good durability in near-neutral water, which is comparable to the best electrocatalysts among known inorganic non-precious metal compounds. The strategy based on the combination of high energy crystalline facets and oxygen vacancies could open a new avenue for designing and developing new and highly efficient electrocatalysts.

Acknowledgments. This work was financially supported by NSFC (51372173, 21173159 and 51420105002), NSFZJ for Distinguished Young Scholars (LR16B010002), Research Climb Plan of ZJED (pd2013383), and Opening Project of State Key Laboratory of High Performance Ceramics and Superfine Microstructure (SKL201409SIC). We thank the High Performance Computing Center of Nanjing University for providing the computing resources.

References

1 J. A. Turner, *Science*, 2004, **305**, 972-974.

2 A. S. Arico, P. Bruce, B. Scrosati, J. M. Tarascon and W. Van Schalkwijk, *Nat. Mater.*, 2005, **4**, 366-377.

3 X. X. Zou and Y. Zhang, *Chem. Soc. Rev*., 2015, **44**, 5148-5180.

4 J. H. Yang, D. E. Wang, H. X. Han and C. Li, *Accounts Chem. Res*., 2013, **46**, 1900-1909.

5 C. Li, X. P. Han, F. Y. Cheng, Y. X. Hu, C. C. Chen and J. Chen, *Nat. Commun*., 2015, **6**, 7345.

6 F. Y. Cheng and J. Chen, *Chem. Soc. Rev*., 2012, **41**, 2172-2192.

7 Q. S. Yin, J. M. Tan, C. Besson, Y. V. Geletii, D. G. Musaev, A. E. Kuznetsov, Z. Luo, K. I. Hardcastle and C. L. Hill, *Science*, 2010, **328**, 342-345.

8 J. Suntivich, K. J. May, H. A. Gasteiger, J. B. Goodenough and Y. Shao-Horn, *Science*, 2011, **334**, 1383-1385.

9 J. Rosen, G. S. Hutchings and F. Jiao, *J. Am. Chem. Soc*., 2013, **135**, 4516-4521.

10 T. Maiyalagan, K. A. Jarvis, S. Therese, P. J. Ferreira and A. Manthiram, *Nat. Commun*., 2014, **5**, 3949.

11 J. Kim, X. Yin, K. C. Tsao, S. H. Fang and H. Yang, *J. Am. Chem. Soc*., 2014, **136**, 14646-14649.

12 A. Grimaud, K. J. May, C. E. Carlton, Y. L. Lee, M. Risch, W. T. Hong, J. G. Zhou and Y. Shao-Horn, *Nat. Commun*., 2013, **4**, 2439.

13 B. M. Hunter, J. D. Blakemore, M. Deimund, H. B. Gray, J. R. Winkler and A. M. Muller, *J. Am. Chem. Soc*., 2014, **136**, 13118-13121.

14 Y. Zhao, R. Nakamura, K. Kamiya, S. Nakanishi and K. Hashimoto, *Nat. Commun*., 2013, **4**, 2390.

15 S. M. Barnett, K. I. Goldberg and J. M. Mayer, *Nat. Chem*., 2012, **4**, 498-502.

16 K. Sardar, S. C. Ball, J. D. B. Sharman, D. Thompsett, J. M. Fisher, R. A. P. Smith, P. K. Biswas, M. R. Lees, R. J. Kashtiban, J. Sloan and R. I. Walton, *Chem. Mater*., 2012, **24**, 4192-4200.

17 M. W. Kanan and D. G. Nocera, *Science*, 2008, **321**, 1072-1075.

18 M. Dincă, Y. Surendranath and D. G. Nocera, *Proc Natl Acad Sci USA*, 2010, **107**, 10337-10341.

19 J. Wu, Y. Xue, X. Yan, W. Yan, Q. Cheng and Y. Xie, *Nano Res*., 2012, **6**, 521-530.

20 T. Takashima, K. Hashimoto and R. Nakamura, *J. Am. Chem. Soc*., 2012, **134**, 1519-1527.

21 K. Jin, J. Park, J. Lee, K. D. Yang, G. K. Pradhan, U. Sim, D. Jeong, H. L. Jang, S. Park, D. Kim, N. E. Sung, S. H. Kim, S. Han, K. T. Nam, *J. Am. Chem. Soc*., 2014, **136**, 7435-7443.

22 Y. W. Liu, C. Xiao, M. J. Lyu, Y. Lin, W. Z. Cai, P. C. Huang, W. Tong, Y. M. Zou and Y. Xie, *Angew. Chem. Int. Ed*., 2015, **54**, 11231-11235.

23 D. K. Ma, S. M. Huang, W. X. Chen, S. W. Hu, F. F. Shi and K. L. Fan, *J. Phys. Chem. C*, 2009, **113**, 4369-4374.

24 S. M. Sun, W. Z. Wang and L. Zhang, *J. Phys. Chem. C*, 2012, **116**, 19413-19418.

25 N. Zhang, R. Ciriminna, M. Pagliaro, Y. Xu, J. *Chem. Soc. Rev*. **2014**, *43*, 5276-5287.

26 L .W. Zhang and Y. F. Zhu, *Catal. Sci. Technol*., 2012, **2**, 694-706.

27 Y. W. Liu, H. Cheng, M. J. Lyu, S. J. Fan, Q. H. Liu, W. S. Zhang, Y. D. Zhi, C. M. Wang, C. Xiao, S. Q. Wei, B. J. Ye and Y. Xie, *J. Am. Chem. Soc*., 2014, **136**, 15670-15675.

28 J. Bao, X. D. Zhao, B. Fan, J. J. Zhang, M. Zhou, W. L. Yang, X. Hu, H. Wang, B. C. Pan and Y. Xie, *Angew. Chem. Int. Ed*., 2015, **54**, 7399-7404.

29 J. H. Huang, J. T. Chen, T. Yao, J. F. He, S. Jiang, Z. H. Sun, Q. H. Liu, W. R. Cheng, F. C. Hu, Y. Jiang, Z. Y. Pan and S. Q. Wei, *Angew. Chem. Int. Ed*., 2015, **54**, 8722-8727.

30 X. Q. Huang, S. H. Tang, H. H. Zhang, Z. Y. Zhou, N. F. Zheng, *J. Am. Chem. Soc*., 2009, **131**, 13916-13917.

31 J. A. Zhang, M. R. Langille, M. L. Personick, K. Zhang, S. Y. Li and C. A. Mirkin, *J. Am. Chem. Soc*., 2010, **132**, 14012-14014.

32 H. Zhang, M. S. Jin and Y. N. Xia, *Angew. Chem. Int. Ed*., 2012, **51**, 7656-7673.

33 B. Y. Xia, H. B. Wu, X. Wang and X. W. Lou, *Angew. Chem. Int. Ed*., 2013, **52**, 12337-12340.

34 C. H. An, J. X. Liu, S. T. Wang, J. Zhang, Z. J. Wang, R. Long and Y. G. Sun, *Nano Energy*, 2014, **9**, 204-211.

35 M. Shang, W. Z. Wang and H. L. Xu, *Cryst. Growth Des*., 2009, **2**, 991-996.

36 G. C. Xi, S. X. Ou, P. Li, J. H. Ye, Q. Ma, N. Su, H. Bai and C. Wang, *Angew. Chem. Int. Ed*., 2012, **51**, 2395-2399.

37 J. Tian, Y. H. Sang, G. W. Yu, H. D. Jiang and X. M. Mu, *Adv. Mater*., 2013, **25**, 5075-5080.

38 Y. Huang, Z. H. Ai, W. K. Ho, M. J. Chen and S. C. Lee, *J. Phys. Chem. C*, 2010, **114**, 6342-6349.

39 Y. Q. Wu and G. X. Lu, *Phys. Chem. Chem. Phys*., 2014, **16**, 4165-4175.

40 Y. Zhou, Z. P. Tian, Z. Y. Zhao, Q. Liu, J. H. Kou, X. Y. Chen, J. Gao, S. C. Yan and Z. G. Zou, *ACS Appl. Mater. Interfaces*, 2011, **3**, 3594-3600.

Graphical Abstract

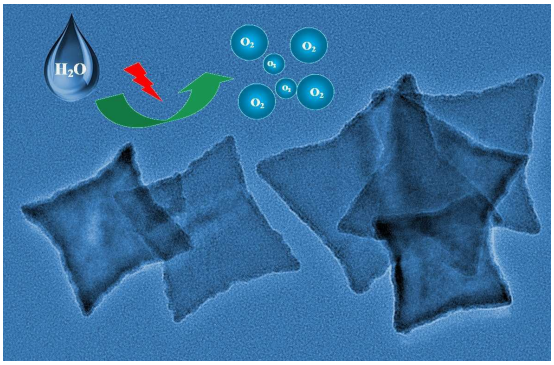

Concave Bi_2WO_6 nanoplates with oxygen vacancies firstly achieved enhanced electrocatalytic oxygen evolution in near-neutral water.